A multi-scale model order reduction scheme for transient modelling of periodic structures

Christophe Droz, Régis Boukadia, Wim Desmet

A multi-scale model order reduction scheme for transient modelling of periodic structures

Christophe Droz[a,c], Régis Boukadia[a,b,c], Wim Desmet[a,c]

[a] *KU Leuven, Department of Mechanical Engineering, Celestijnenlaan 300, Heverlee, Belgium*
[b] *École Centrale de Lyon, LTDS - CNRS UMR 5513, Ecully, France*
[c] *DMMS Lab, Flanders Make, Belgium*

Abstract

In this paper, a Floquet Model Order Reduction (MOR) method is proposed for the modelling of finite periodic structures subjected to harmonic or transient loads. This Floquet MOR generates frequency-independent projection matrices of the full-scale structure using a Floquet expansion of the local state-vectors computed on a single unit-cell with the Forced Wave Finite Element framework. This two-step MOR method can handle large multi-scale waveguides regardless of the scale and the number of unit-cells. A comparison with a standard sub-structuring approach based on unit-cell wave-mode reduction demonstrates that Floquet MOR is able to create reduced models of finite periodic structures with an unequaled computational efficiency. The method's ability to produce small and accurate models suitable for time-domain simulations presents a high potential for virtual sensing, real-time Structural Health Monitoring (SHM) and digital twins for large periodic structures and metamaterials.

Keywords: Periodic structure, Transient Modelling, Wave Finite Element, Model Order Reduction, Multiscale, Floquet-Bloch theory

1. Introduction

The requirement for high-fidelity models describing the structural dynamics and acoustic behavior of engineering structures increases with our society's growing concern for human safety and comfort. Indeed, the development of scalable materials and meta-structures capable of combining high structural integrity with vibroacoustic performances has been exerting a considerable pressure on the computational requirements in fields such as model-based Noise and Vibration Harshness (NVH) and predictive Structural Health Monitoring (SHM). To address these computational performances issues, Model Order Reduction (MOR) and sub-structuring techniques have been used for dynamic systems as early as in the 60s with the works of Hurty [1] on modal decomposition in order to produce displacement transformation matrices for Component Mode Synthesis (CMS). Reviews by Besselink et al.[2] and Klerk et al.[3] provide a history and relevant classification techniques for general sub-structuring and MOR techniques.

Email address: christophe.droz@gmail.com (Christophe Droz)

Nowadays, an emphasis is being put on time domain applications of MOR and dynamic sub-structuring techniques. A detailed survey of projection-based MOR was proposed by Lulf et al.[4] for discrete non-linear problems. A typical example is the interaction of a dynamic system with a 'hard' non-linearity (e.g. contact, friction), which may induce chaotic responses that cannot generally be studied with non-linear frequency methods (e.g harmonic balance method (HBM)). In damage detection and broader SHM applications, Fourier transform can sometimes be used to unlock efficient frequency-domain MOR, but remains mostly limited to steady-state linear (or linearizable) systems with time invariant parameters. The same limitations exist for the development and exploitation of digital twins. Kapteyn et al.[5] used component-based MOR to build a physics-based near-real-time digital twin, aiming for a drone's ability to perform autonomous SHM. Time-domain MOR is also critical in the field of virtual sensing, were real-time state/input estimations methods are needed for certain vibroacoustic applications (e.g. see [6, 7, 8]). Such applications are particularly challenging when the models' outputs require a high level of spatial resolution across a large-scale structure. It is then crucial for a MOR strategy to produce small and accurate models which are actionable via direct time integration.

Modal projection methods such as CMS are popular for reducing large dynamic systems, as the resulting Reduced-Order Model (ROM) is generally exploitable in both frequency- and time-domains. When a large structure is made of an assembly of many sub-components, multi-scale MOR methods are needed to circumvent the computation of global modes and solve smaller eigenvalue problems. In model-based SHM and vibro-acoustic applications, multi-scale problems are often due to the co-existence of a macroscopic structure and a periodic architecture at the micro- or meso-scale (e.g. meta-materials, lattices, thin-walled or stiffened plates). To exploit their repetitive nature, periodic structure theory has been used to compute the dynamic response of periodic media based on a refined finite element (FE) description of their unit-cell [9]. The Wave Finite Element Method (WFEM) is a popular implementation allowing the computation of the finite response of loaded waveguides under different boundary conditions. Its interest lies in the reduction of the overall system into a considerably smaller set of propagating and evanescent wave amplitudes, which are resulting from a Floquet expansion of the displacements and forces state-vectors. The final system's dimension is independent of the number of unit-cells (UCs) in the structure. A reduced formulation of this Forced WFEM was investigated in Boukadia et al.[10] to explore wave localization effects in a stiffened plate. However the main drawback of this Forced WFEM framework is the underlying periodicity assumption of the Floquet expansion, which makes the WFEM incompatible with most valuable time-domain applications. Recently some authors [11, 12] used Inverse Fourier Transform to achieve time domain analyses of periodic structures, thus using the method's outstanding performances for harmonic analyses to predict their transient response. Unfortunately, this approach is not compatible with real-time model estimation and updating, which are crucial for digital twin or virtual sensing applications.

Modal projection techniques have been used at the unit-cell scale in combination with the Periodic structure theory, to reduce the size of spectral eigenvalue problems and accelerate the computation of wave dispersion characteristics. Different techniques were proposed to build the local projection matrices: a combination of a component modes with a subset of least evanescent wave vectors were used by Droz et al.[13, 14] to reduce the interior and boundaries of the

periodic unit-cells. As an alternative to wave vectors, Krattinger and Hussein [15] adapted the CMS to Floquet-Bloch conditions and extended interior CMS reduction with boundary modes. A variety of similar techniques were proposed to generate a ROM for periodic UCs in order to compute their dispersion characteristics with 1D or 2D periodic finite element frameworks [16, 17, 18]. These methods are often qualified as 'UC MOR', as the local modes and waves derived from the UCs are used to build a UC projection matrix, but do not take into account the global loads or boundary conditions of the overall structure. Still, a local MOR approach can be used to assemble a global projection matrix (see for example [19, 20]), later used to reduce the finite structure and compute its dynamic response under various boundary conditions. For example, Hu and Oskay [21] used a truncated local modal basis to create a frequency independent projection matrix. The global system built by assembling the local projection matrices was then used to conduct transient simulations in a large-scale phononic meta-material. Although these approaches, referred as 'Local MOR' in this paper, only require a single UC to build the projection matrix, the periodic nature of the structure is not fully exploited at the macro-scale, and the dimension of the global ROM always grows with the number of UCs.

To summarize, two approaches based on UC analysis have been investigated to build the ROM of periodic waveguides, suitable for time-domain simulations: (i) the Periodic Structure Theory, which is a highly efficient way to reduce a periodic system regardless the number of UCs. However it relies on a frequency-dependent projection inherent to the state vector's expansion onto Floquet vectors. (ii) the 'Local MOR' approach, which takes advantage of local modes and wave solutions to build a reduced UC ROM, later assembled to create a global projection matrix. However the dimension of the global system depends on the number of UCs hence it does not fully take advantage of the structure's periodicity.

In this paper, a two-step strategy is proposed for generating a macro-scale ROM, actionable in time-domain while being based on Floquet theory and reduced UC analysis. Sections 2.1 and 2.2 remind the formalism and highlight the methodological and conceptual differences between Floquet expansion and local MOR methods for computing the dynamic response of finite periodic structures. In section 2.3 a Floquet MOR approach is introduced to generate global projection matrices from the expansion of forced state vectors computed using reduced UCs. The pros and cons of local MOR and Floquet MOR are discussed in section 3, with a thorough comparison of their numerical performances with regards to model size and UC scaling. In section 4 the Floquet MOR and an implicit integration scheme are used to study the impulse response of a periodic structure with 2D elliptic inclusions. The possible limitations of the method when it comes to high-frequency contents are stressed and conclusions are drawn in section 5.

2. Formulation of the model-order reduction scheme for periodic structures

2.1. Wave Finite Element Framework for dynamic analyses

Let us first remind the numerical formalism used to model a finite periodic structure based on Floquet theory and UC finite elements. Consider a linear elastic structure made of repetitive cells along one direction. The governing

equation of the overall system writes:

$$\mathcal{M}\frac{\partial^2\mathcal{U}(t)}{\partial t^2}+\mathcal{C}\frac{\partial\mathcal{U}(t)}{\partial t}+\mathcal{K}\,\mathcal{U}(t)=\mathcal{F}(t) \tag{1}$$

where cursive $\mathcal{M}$, $\mathcal{C}$ and $\mathcal{K}$ stand for the assembled FE mass, damping and stiffness matrices of the system, while $\mathcal{U}(t)$ and $\mathcal{F}(t)$ are the global nodal displacements and external forces. Assuming the structure is made of 'N' identical cells with compatible meshes, the FE model of a single sub-structure of index 'n' can be used to describe the force equilibrium in the absence of inner loads:

$$\begin{bmatrix}\mathbf{M}_{LL} & \mathbf{M}_{LI} & \mathbf{M}_{LR}\\ \mathbf{M}_{IL} & \mathbf{M}_{II} & \mathbf{M}_{IR}\\ \mathbf{M}_{RL} & \mathbf{M}_{RI} & \mathbf{M}_{RR}\end{bmatrix}\frac{\partial^2}{\partial t^2}\begin{Bmatrix}\mathbf{U}_L^{(n)}\\ \mathbf{U}_I^{(n)}\\ \mathbf{U}_R^{(n)}\end{Bmatrix}(t)+\begin{bmatrix}\mathbf{C}_{LL} & \mathbf{C}_{LI} & \mathbf{C}_{LR}\\ \mathbf{C}_{IL} & \mathbf{C}_{II} & \mathbf{C}_{IR}\\ \mathbf{C}_{RL} & \mathbf{C}_{RI} & \mathbf{C}_{RR}\end{bmatrix}\frac{\partial}{\partial t}\begin{Bmatrix}\mathbf{U}_L^{(n)}\\ \mathbf{U}_I^{(n)}\\ \mathbf{U}_R^{(n)}\end{Bmatrix}(t)+\begin{bmatrix}\mathbf{K}_{LL} & \mathbf{K}_{LI} & \mathbf{K}_{LR}\\ \mathbf{K}_{IL} & \mathbf{K}_{II} & \mathbf{K}_{IR}\\ \mathbf{K}_{RL} & \mathbf{K}_{RI} & \mathbf{K}_{RR}\end{bmatrix}\begin{Bmatrix}\mathbf{U}_L^{(n)}\\ \mathbf{U}_I^{(n)}\\ \mathbf{U}_R^{(n)}\end{Bmatrix}(t)=\begin{Bmatrix}\mathbf{F}_L^{(n)}\\ \mathbf{0}\\ \mathbf{F}_R^{(n)}\end{Bmatrix}(t) \tag{2}$$

where $\mathbf{M}$, $\mathbf{C}$ and $\mathbf{K}$ are the assembled FE mass, damping and stiffness matrices of the UC, while the sub-scripts 'L', 'I', 'R' stand for left-, inner- and right-sided degrees of freedom (DOF), respectively. Uppercase $\mathbf{U}(t)$ and $\mathbf{F}(t)$ denote the cell's nodal displacements and external forces.

In harmonic regime, the governing equation of the global system writes $\mathcal{D}(\omega)\mathcal{U}(\omega)=\mathcal{F}(\omega)$, where $\mathcal{D}=\mathcal{K}+j\omega\mathcal{C}-\omega^2\mathcal{M}$. Using Floquet theory provides the solution $U(x)$ of a linear system of equations $H(x)U(x)=0$ where H is a periodic operator such as $H(x+d)=H(x)$. The solution can decomposed with Floquet vectors as: $U(x)=\mathbb{V}(x)e^{\kappa x}$ where κ is a constant matrix and $\mathbb{V}$ is an invertible d-periodic matrix. In the following, Ψ denotes the wave matrices and $\lambda=e^{\kappa d}$ are the Floquet coefficients (i.e. propagation constants), used to relate the consecutive state-vectors of the UC's displacements:

$$\begin{Bmatrix}\mathbf{u}_L^{(n+1)}\\ \mathbf{u}_I^{(n+1)}\end{Bmatrix}=\lambda\begin{Bmatrix}\mathbf{u}_L^{(n)}\\ \mathbf{u}_I^{(n)}\end{Bmatrix} \tag{3}$$

Introducing the periodicity conditions between two consecutive UCs, using the above mentioned state-vectors yields the following spectral eigenproblem:

$$\mathbf{D}(\lambda)\begin{Bmatrix}\mathbf{u}_L\\ \mathbf{u}_I\end{Bmatrix}=\begin{Bmatrix}\mathbf{0}\\ \mathbf{0}\end{Bmatrix} \tag{4}$$

where $\mathbf{D}$ is the cell's dynamic stiffness matrix and:

$$\mathbf{D}(\lambda)\ :\ \mathbf{D}\longrightarrow\begin{bmatrix}\mathbf{D}_{RL} & \mathbf{D}_{RI}\\ \mathbf{0} & \mathbf{0}\end{bmatrix}\frac{1}{\lambda}+\begin{bmatrix}\mathbf{D}_{RR}+\mathbf{D}_{LL} & \mathbf{D}_{LI}\\ \mathbf{D}_{IL} & \mathbf{D}_{II}\end{bmatrix}+\begin{bmatrix}\mathbf{D}_{LR} & \mathbf{0}\\ \mathbf{D}_{IR} & \mathbf{0}\end{bmatrix}\lambda$$

Note that with the WFEM, a dynamic condensation is usually achieved to simplify the quadratic eigenvalue problem (EVP) into the common expression:

$$\left(\lambda\mathbb{D}_{LR}+(\mathbb{D}_{LL}+\mathbb{D}_{RR})+\frac{1}{\lambda}\mathbb{D}_{RL}\right)\mathbf{u}_L=\mathbf{0} \tag{5}$$

where blackboard bold $\mathbb{D} = \mathbf{D}_{b,b} - \mathbf{D}_{b,I}\mathbf{D}_{II}^{-1}\mathbf{D}_{I,b}$ stands in the following for the condensed cell's matrix with sub-script notation $b = \{L, R\}$.

A variety of numerical schemes [22] can be used to solve Eq.(5). One of the major features of WFEM lies in the straightforwardness of boundary conditions implementation for determining the finite waveguide's dynamic response. Indeed, the multi-modal wave expansion can be written to decompose any state vector's displacements $\mathbf{u}_L^{(n)}$ using the solutions of Eqs.(5) or (4), sorted into positive- and negative- going (ψ^+, ψ^-) eigenvectors and their respective propagation constants as:

$$\mathbf{u}^{(n)} = \sum_{s=1}^{S} \left(\lambda_s^n \psi_s^+ \mathbf{q}_s^+ + \lambda_s^{N-n} \psi_s^- \mathbf{q}_s^- \right) \tag{6}$$

where $\mathbf{q}^+$ and $\mathbf{q}^-$ are the complex wave amplitudes and 'S' the number of solutions retained in the decomposition.

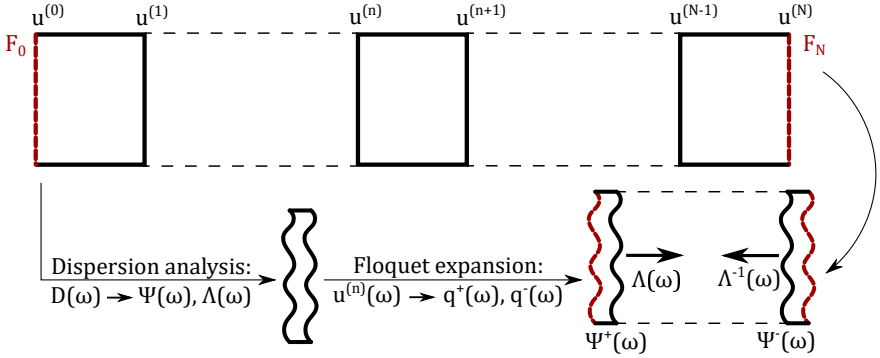

Figure 1: Concept diagram of the forced WFEM.

Considering the free-free waveguide configuration, the force equilibrium on both sides subjected respectively to $\mathbf{F}_0$ and $\mathbf{F}_N$ yields the following system of equations, where Ψ are the concatenated eigenvectors and Λ the diagonal eigenvalues matrix:

$$\begin{bmatrix} \mathbb{D}_{LL}\Psi^+ + \mathbb{D}_{LR}\Psi^+\Lambda & \mathbb{D}_{LL}\Psi^-\Lambda^N + \mathbb{D}_{LR}\Psi^-\Lambda^{N-1} \\ \mathbb{D}_{RL}\Psi^+\Lambda^{N-1} + \mathbb{D}_{RR}\Psi^+\Lambda^N & \mathbb{D}_{RL}\Psi^-\Lambda + \mathbb{D}_{RR}\Psi^- \end{bmatrix} \begin{Bmatrix} \mathbf{q}^+ \\ \mathbf{q}^- \end{Bmatrix} = \begin{Bmatrix} \mathbf{F}_0 \\ \mathbf{F}_N \end{Bmatrix} \tag{7}$$

Solving Eq.(7), nodal displacements can be derived at any cell (n) using Eq.(6). Note that the size of Eq.(7) is twice the number of DOF in a state vector and does not depend on the number of UCs in the overall structure. It is also worth mentioning that the computation effort mainly lies in the determination of the frequency-dependent wave-modes Ψ and propagation constants Λ. Then, the dynamic response of the periodic structure with various boundary conditions or number of UCs can be determined.

2.2. Local MOR based on reduced unit-cell analysis

The above formulation allows a drastic reduction of the dynamic system's size. However, the Floquet expansion is based on the spatial periodicity of the dynamic operator, which is only valid in harmonic regime. The projection is

therefore based on frequency dependent entities hence is not suitable for the reduction of the system in time domain.

In the following, the local modes of the UC are used to build a global projection matrix of the periodic structure. This corresponds to the so-called Local MOR and can be seen as a multi-scale sub-structuring technique taking advantage of the periodicity to reuse a same reduction basis for each UC. The governing equation of each UC (i.e. Eq.(2)) is reduced by creating a local projection matrix Γ such that Eq.(2) becomes:

$$\begin{cases} \Gamma^* \mathbf{M} \Gamma \dfrac{\partial^2 \mathbf{p}^{(n)}(t)}{\partial t^2} + \Gamma^* \mathbf{C} \Gamma \dfrac{\partial \mathbf{p}^{(n)}(t)}{\partial t} + \Gamma^* \mathbf{K} \Gamma \, \mathbf{p}^{(n)}(t) = \Gamma^* \, \mathbf{F}^{(n)}(t) \\ \begin{Bmatrix} \mathbf{u}_L^{(n)} \\ \mathbf{u}_I^{(n)} \\ \mathbf{u}_L^{(n+1)} \end{Bmatrix} = \Gamma \, \mathbf{p}^{(n)}(t) \end{cases} \tag{8}$$

Several reduction techniques were proposed to find a suitable local projection matrix to reduce the UCs, which can be seen a specific application of more general modal sub-structuring approaches. The periodic nature of the media provides a straightforward dividing where either normal and constrained modes or even wave-modes can be used to describe the inner cells' dynamics.

In the following a reduction of the UCs is achieved using a two-step approach. In harmonic regime, Eq.(2) writes:

$$\begin{bmatrix} \mathbf{D}_{LL} & \mathbf{D}_{LI} & \mathbf{D}_{LR} \\ \mathbf{D}_{IL} & \mathbf{D}_{II} & \mathbf{D}_{IR} \\ \mathbf{D}_{RL} & \mathbf{D}_{RI} & \mathbf{D}_{RR} \end{bmatrix} (\omega) \begin{Bmatrix} \mathbf{u}_L^{(n)} \\ \mathbf{u}_I^{(n)} \\ \mathbf{u}_L^{(n+1)} \end{Bmatrix} (\omega) = \begin{Bmatrix} \mathbf{f}_L^{(n)} \\ \mathbf{0} \\ -\mathbf{f}_L^{(n+1)} \end{Bmatrix} (\omega) \tag{9}$$

The inner displacement DOF $\mathbf{u}_I^{(n)}$ of the UC can be approximated using a Component Mode Synthesis as follows:

$$\mathbf{u}_I^{(n)}(\omega) \approx \Phi_s \mathbf{p}_s^{(n)}(\omega) + \Phi_c \mathbf{p}_c^{(n)}(\omega) \tag{10}$$

where the static modes $\Phi_s = [\mathbf{\Phi_{s|_L}} \mathbf{\Phi_{s|_R}}]$ (i.e. constrained interface modes) are calculated by:

$$\Phi_s = -\mathbf{K}_{II}^{-1} \begin{bmatrix} \mathbf{K}_{IL} & \mathbf{K}_{IR} \end{bmatrix} \tag{11}$$

while the component modes are obtained selecting a truncated set of modal eigenvalues as shown in Eq.(12). Note that the specification of a frequency limit criterion $\omega_{\max}$ is necessary:

$$\begin{cases} \left(\mathbf{K}_{II} - \nu_j \mathbf{M}_{II} \right) \phi_j = \mathbf{0} \\ \Phi_c \mathbf{p}_c = \displaystyle\sum_{j \in \Omega} \phi_j p_{c,j} \quad ; \quad \Omega = \left\{ j, \nu_j \leq \omega_{\max}^2 \right\} \end{cases} \tag{12}$$

Krylov decomposition [23] can be advantageously used to implement the Arnoldi algorithm required to solve Eq.(12), given the problem's sparsity. Solutions are retained up to $\nu_i \geq \omega_p^2$, the maximal frequency above which modes are truncated. This frequency-dependent criterion is an important parameter impacting the overall size of the

reduced model. The following (frequency-independent) projection matrix can be used to reduce the inner DOF of each UC's state vectors:

$$\begin{Bmatrix} \mathbf{u}_L^{(n)} \\ \mathbf{u}_I^{(n)} \\ \mathbf{u}_L^{(n+1)} \end{Bmatrix}(\omega) = \begin{bmatrix} \mathbf{I} & \mathbf{0} & \mathbf{0} \\ \mathbf{\Phi_{s|_L}} & \mathbf{\Phi_c} & \mathbf{\Phi_{s|_R}} \\ \mathbf{0} & \mathbf{0} & \mathbf{I} \end{bmatrix} \begin{Bmatrix} \mathbf{u}_L^{(n)} \\ \mathbf{p_c}^{(n)} \\ \mathbf{u}_L^{(n+1)} \end{Bmatrix}(\omega) \tag{13}$$

This approach was used effectively in several sub-structuring and homogenization techniques. However, the interfaces between the UCs are not affected by the CMS, although a variety of modal descriptions have been investigated to reduce the cells' edges. In the context of a wave-based modelling of the structure, Floquet solutions (i.e. wave shapes computed by WFEM) can be used as an efficient way to describe the state vectors of a UC. The concept of Floquet state-vector reduction for dispersion analyses was introduced in [13] then improved in [10] by using the inverse WFEM formulation to speed up solution sub-set computation and include evanescent waves' contribution in the reduced model. The goal is to propose a frequency-independent projection matrix $\mathbf{\Psi_w}$ to replace the edge state-vector $\mathbf{u}_L^{(n)}$ by a reduced one $\mathbf{p}_L^{(n)}$. Interested reader can also refer to [17] for other examples of MOR for the WFEM. For a sake of completeness, a state-vector reduction procedure (detailed in [10]) is summarized below:

- The first step is to identify the partial contours of the Brillouin zone. It can be done using one direct (for $\lambda(\omega_{max})$) and one inverse (for $\omega(\{|\lambda| = 1\})$) resolution of the spectral eigenproblem, using the UC element matrices,
- Then, a wavenumber sampling can be defined and used to solve the inverse (wavenumber-dependent) eigenproblems,
- The real and imaginary parts of each state-vector is collected to build a reduced solution subspace, using a SVD procedure,
- Eventually, one can build the wave projection basis Ψ_w for each cell's edge $\mathbf{u}_L^{(n)}$, so that the displacement state-vectors can be written:

$$\mathbf{u}_L^{(n)}(\omega) = \mathbf{\Psi_w}\mathbf{p}_L^{(n)}(\omega) \tag{14}$$

The local projection matrix Γ defined in Eq.(8) for the overall UC is then written:

$$\Gamma = \begin{bmatrix} \mathbf{\Psi_w} & \mathbf{0} & \mathbf{0} \\ \mathbf{\Phi_{s|_L}} & \mathbf{\Phi_c} & \mathbf{\Phi_{s|_R}} \\ \mathbf{0} & \mathbf{0} & \mathbf{\Psi_w} \end{bmatrix} \tag{15}$$

The global projection matrix can eventually be assembled using the local scale projection matrices as detailed in Eq.(16). This local MOR approach is synthesized in Fig.2.

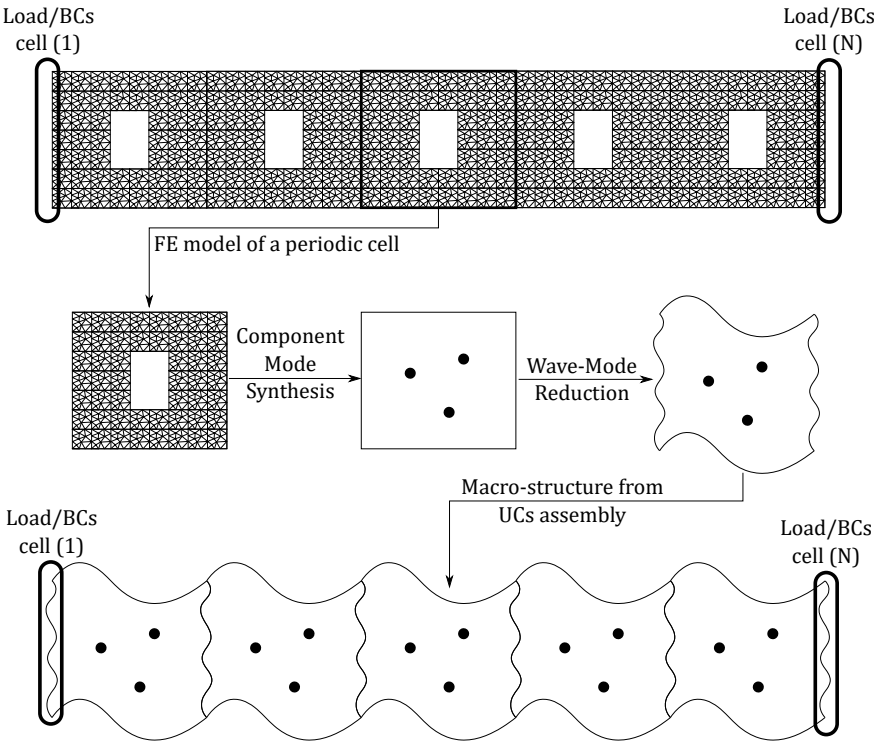

Figure 2: Concept diagram for the Local MOR method. Local ROM is replicated for each UC in the structure and does not depend on the boundary conditions or load case.

$$\mathcal{U}(t) = \begin{Bmatrix} \mathbf{U}_L^{(0)} \\ \mathbf{U}_I^{(0)} \\ \vdots \\ \mathbf{U}_L^{(n)} \\ \mathbf{U}_I^{(n)} \\ \mathbf{U}_L^{(n+1)} \\ \vdots \\ \mathbf{U}_L^{(N)} \end{Bmatrix} (t) = \begin{bmatrix} \boldsymbol{\Psi}_\mathbf{w} & \mathbf{0} & \mathbf{0} & & & & & \\ \boldsymbol{\Phi}_{\mathbf{s}|_\mathbf{L}} & \boldsymbol{\Phi}_\mathbf{c} & \boldsymbol{\Phi}_{\mathbf{s}|_\mathbf{R}} & & & & & \\ & & \ddots & & & & & \\ & & & \boldsymbol{\Psi}_\mathbf{w} & \mathbf{0} & & & \\ & & & \boldsymbol{\Phi}_{\mathbf{s}|_\mathbf{L}} & \boldsymbol{\Phi}_\mathbf{c} & \boldsymbol{\Phi}_{\mathbf{s}|_\mathbf{R}} & & \\ & & & & \mathbf{0} & \boldsymbol{\Psi}_\mathbf{w} & & \\ & & & & & & \ddots & \\ & & & & & & \mathbf{0} & \boldsymbol{\Psi}_\mathbf{w} \end{bmatrix} \begin{Bmatrix} \mathbf{P}_w^{(0)} \\ \mathbf{P}_c^{(0)} \\ \vdots \\ \mathbf{P}_w^{(n)} \\ \mathbf{P}_c^{(n)} \\ \mathbf{P}_w^{(n+1)} \\ \vdots \\ \mathbf{P}_w^{(N)} \end{Bmatrix} (t) = \mathcal{B}\mathcal{P}(t) \tag{16}$$

The main advantages of Local MOR are its ease of computation (size of a single UC) and the fact that the resulting basis is intrinsically frequency-independent. However the drawback of Local MOR reduction arises when the number of local modes, waves or UCs is high: the dimension of the reduced model is the product of the number of local modes and waves by the number of UCs. Consequently, a large number of UCs may produce an excessively large reduction basis, while an insufficient number of UCs may be responsible for an inaccurate model. Moreover, Local MOR does not take into account the specific loads or boundary conditions hence generates a sub-optimal reduction basis.

2.3. Formulation of a global MOR based on the Floquet expansion of forced WFEM state-vectors

Note however that Local MOR can be used prior to the Floquet expansion described in Eq.(7). In this case, the modal basis can be over-determined without consequences on the final number of unknown wave amplitudes $\mathbf{q}^{+}(\omega)$ and $\mathbf{q}^{-}(\omega)$. The main advantage of WFEM remains, which is to provide fast dynamic response to a given load or BCs, disregarding the number of UCs composing the periodic structure. Its limitation lies in the frequency-dependence of the wave-modes derived from the spectral eigenproblem. This drawback will be tackled using a snapshot-type Proper Orthogonal Decomposition technique, to generate a low dimension model approximating the waveguide's dynamics from a subset of full state vectors' responses computed using WFEM. An illustration of the strategy is displayed in Fig.3.

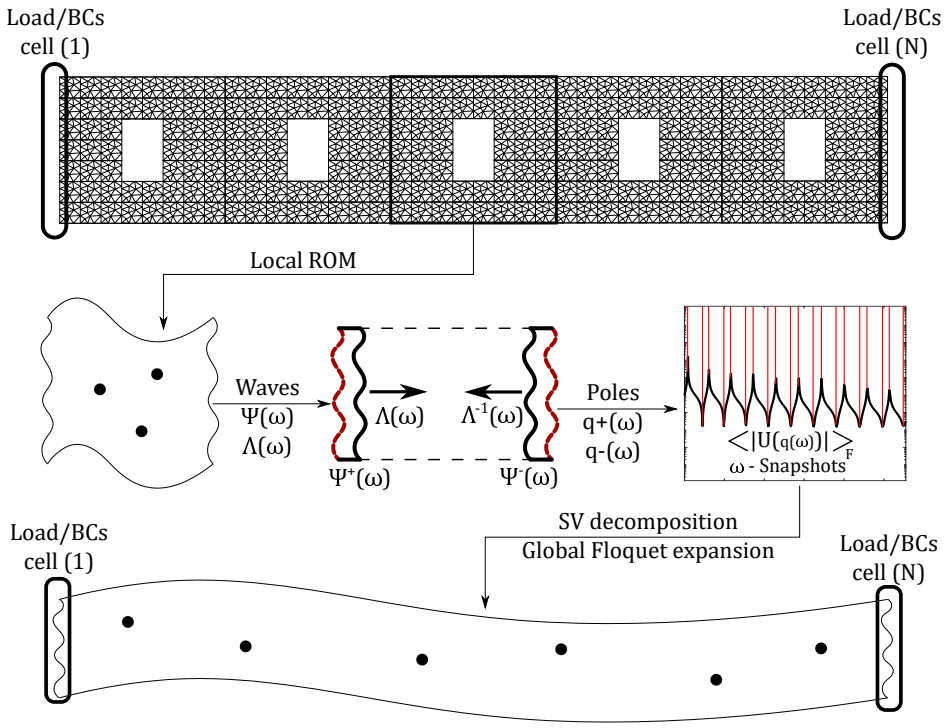

Figure 3: Concept diagram for the Floquet MOR, exploiting Forced WFEM with a POD-like technique to generate global projection matrix from a Floquet expansion of the UC state-vectors.

The local projection matrix is first re-arranged from Eq.(15), so that the state vectors write:

$$\begin{Bmatrix} \mathbf{u}_L^{(n)} \\ \mathbf{u}_I^{(n)} \\ \mathbf{u}_L^{(n+1)} \end{Bmatrix}(\omega) = \begin{bmatrix} \boldsymbol{\Psi} & \mathbf{0} & \mathbf{0} \\ \boldsymbol{\Phi}_{\mathbf{s}|_\mathbf{L}} & \boldsymbol{\Phi}_{\mathbf{s}|_\mathbf{R}} & \boldsymbol{\Phi}_\mathbf{c} \\ \mathbf{0} & \boldsymbol{\Psi} & \mathbf{0} \end{bmatrix} \begin{Bmatrix} \mathbf{p}_L^{(n)} \\ \mathbf{p}_L^{(n+1)} \\ \mathbf{p}_I^{(n)} \end{Bmatrix}(\omega) \tag{17}$$

The dynamic stiffness matrices are then reduced using the above projection: $\tilde{\mathbf{D}} = \Gamma^{*}\mathbf{D}\Gamma$. Note that neither the number of modes used to describe the inner cell's dynamic, nor the number of waves used to describe the cell's edges

contribute to the final ROM dimension. Both selection constraints can be loosen with minor consequences to the overall performances of the MOR algorithm. A condensation of the inner DOF (i.e. component modes of the UC) can be achieved to define the dynamic stiffness matrix $\mathbb{D}$:

$$\mathbb{D} = \begin{bmatrix} \tilde{\mathbf{D}}_{LL} & \tilde{\mathbf{D}}_{LR} \\ \tilde{\mathbf{D}}_{RL} & \tilde{\mathbf{D}}_{RR} \end{bmatrix} - \begin{bmatrix} \tilde{\mathbf{D}}_{LI} \\ \tilde{\mathbf{D}}_{RI} \end{bmatrix} \left[\tilde{\mathbf{D}}_{II}\right]^{-1} \begin{bmatrix} \tilde{\mathbf{D}}_{IL} & \tilde{\mathbf{D}}_{IR} \end{bmatrix} \tag{18}$$

The condensed form of the direct spectral problem defined in Eq.(5) is solved to assemble the (frequency-dependent) reduced wave solutions $\boldsymbol{\Psi}^{+}(\omega)$, $\boldsymbol{\Psi}^{-}(\omega)$ and the diagonal propagation constants' matrix $\boldsymbol{\Lambda}(\omega)$. The forced response system is then built using the WFEM framework (i.e. Eq.(7) for a free end waveguide). The solution is derived as a couple of complex wave amplitudes $\mathbf{q}^{+}(\omega)$ and $\mathbf{q}^{-}(\omega)$. The selection of appropriate snapshots to be later used for a computationally efficient proper orthogonal decomposition can be achieved using different heuristics (e.g. modal energy, error minimization). In this paper, the poles of the frequency response function averaged on each node subjected to external load are used to generate the snapshots. The key advantage of WFEM lies in its extremely low computational effort for punctual FRF determination, which allows a direct identification of resonances and anti-resonances of the finite structure. Let us denote $\Omega = \{\omega_i\}_{0 \leq i \leq N_f}$ the frequency snapshots' subset collecting the poles of the loaded waveguide. Note that the global state vectors do not have to be computed to identify the poles (nor does the global dynamic stiffness matrix). The small number of snapshots N_f allows a fast collection of a equal number of reduced edge state vectors $\mathbf{p}_L$ using the Floquet expansion, defined for UC index 'n' at each frequency ω_i by:

$$\mathbf{p}_L^{(n)}(\omega_i) = \boldsymbol{\Psi}^{+}(\omega_i)\, \boldsymbol{\Lambda}^{n}(\omega_i)\, \mathbf{q}^{+}(\omega_i) + \boldsymbol{\Psi}^{-}(\omega_i)\, \boldsymbol{\Lambda}^{N-n}(\omega_i)\, \mathbf{q}^{-}(\omega_i) \tag{19}$$

while the inner part $\mathbf{p}_I$ of the reduced state vectors can be obtained using Eq.(18):

$$\mathbf{p}_I^{(n)}(\omega_i) = \left[\tilde{\mathbf{D}}_{II}\right]^{-1} \left[\tilde{\mathbf{D}}_{IL}\, \mathbf{p}_L^{(n)}(\omega_i) \quad \tilde{\mathbf{D}}_{IR}\, \mathbf{p}_L^{(n+1)}(\omega_i)\right] \tag{20}$$

The local displacement state vectors $\mathbf{u}^{(n)}$ can then be retrieved using Eq.(17). The organised global state vectors are collected into the expanded snapshot matrix $\mathbb{U}_\Omega$ as follows:

$$\mathbb{U}_\Omega = \left\{ \underbrace{\begin{Bmatrix} \mathbf{u}_L^{(0)} \\ \mathbf{u}_I^{(0)} \\ \vdots \\ \mathbf{u}_I^{(N-1)} \\ \mathbf{u}_L^{(N)} \end{Bmatrix}}_{\omega_1}, \underbrace{\begin{Bmatrix} \mathbf{u}_L^{(0)} \\ \mathbf{u}_I^{(0)} \\ \vdots \\ \mathbf{u}_I^{(N-1)} \\ \mathbf{u}_L^{(N)} \end{Bmatrix}}_{\omega_2}, \cdots, \underbrace{\begin{Bmatrix} \mathbf{u}_L^{(0)} \\ \mathbf{u}_I^{(0)} \\ \vdots \\ \mathbf{u}_I^{(N-1)} \\ \mathbf{u}_L^{(N)} \end{Bmatrix}}_{\omega_{N_f}} \right\} \tag{21}$$

The dimensions of matrix $\mathbb{U}_\Omega$ generally make it advantageous to use Lanczos bi-diagonalization with a partial re-orthogonalization [24] to achieve an computationally efficient singular value decomposition where the snapshot matrix writes:

$$\mathbb{U}_\Omega = \mathbb{V}\, \boldsymbol{\Sigma}\, \mathbb{W}^{H} \tag{22}$$

where $\mathbf{\Sigma}$ is a diagonal matrix containing the sorted singular values of the decomposition. A truncation is achieved to a limited number 'r' of singular values using a residue minimum defined by:

$$\sum_{i=1}^{R} \sigma_i > (1-\epsilon)\,\mathrm{Tr}\,(\mathbf{\Sigma}) \tag{23}$$

Note that in the general case, one has $r \leq N_f$, although the combination of an accurate pole identification (which produces reliable snapshots) and a low specified residue $\epsilon \longrightarrow 0$ can yield $r = N_f$, which becomes the final dimension of the reduced macro-scale model. The projection matrix is therefore assembled using the r columns-elements of $\mathbb{V}$ as:

$$\mathcal{B} = \left[\mathbb{V}_{\sigma_1} \quad , \ldots , \quad \mathbb{V}_{\sigma_r}\right] \tag{24}$$

The projection matrix $\mathcal{B}$ should be recomputed if the boundary conditions are modified. The force boundary condition (described in Eq.(7)) is the most general case, since other boundary conditions can be written similarly after achieving a dynamic condensation of the constrained edge element to the subsequent ($n = 1$) or second to last ($n = N - 1$) cell. The use of explicit displacement- or force-based edge conditions can however prove advantageous when large UCs are considered. The global system defined in time domain by Eq.(1) becomes after Floquet MOR:

$$\begin{cases} \mathcal{B}^* \mathcal{M} \mathcal{B}\, \dfrac{\partial^2 \mathbf{p}(t)}{\partial t^2} + \mathcal{B}^* \mathcal{C} \mathcal{B}\, \dfrac{\partial \mathbf{p}(t)}{\partial t} + \mathcal{B}^* \mathcal{K} \mathcal{B}\, \mathbf{p}(t) = \mathcal{B}^*\, \mathcal{F}(t) \\ \mathcal{U}(t) = \mathcal{B}\, \mathbf{p}(t) \end{cases} \tag{25}$$

where $\mathbf{p}(t)$ is a reduced variable of dimension 'r'. The reduction parameters and numerical performances of the two methods are discussed in next section.

3. Discussion on numerical aspects and performances of Local and Floquet MOR

3.1. Comparison of modeling strategies and reduction parameters

Before analysing the method's accuracy for time-domain applications, let us discuss some sensitive numerical aspects of the proposed reduction scheme. Indeed, UC reduction is classically meant to accelerate the computation of dispersion curves, hence its performances are often solely discussed in terms of accuracy of the wave dispersion characteristics (e.g. wavenumbers) and compared for different UCs' meshes or geometries. These do not constitute a relevant benchmark for addressing finite structures. In that sense, Local MOR described in Sec.2.2 can be seen as a direct extension of existing UC reduction techniques for the construction of a global frequency-independent projection matrix, to be later used for time domain analysis. The local MOR and the FEM will both be compared to the Floquet MOR introduced in Sec.2.3, which also uses local UC reduction prior to the creation of a global projection basis, but now resulting from a Floquet expansion onto the entire structure. The finite nature of the structure means that Floquet MOR is affected differently by the UC reduction parameters than the Local MOR, as the number of UCs is not linked to the minimum number of required Floquet expanders. A reasonable hypothesis is that the local MOR

will prove more efficient than Floquet MOR for structures constituted of a small number of large UCs, while Floquet MOR will become advantageous as the structure involves an increasingly large number of small UCs. To conduct a fair comparison between these MOR strategies and evaluate our method, let us consider the following parametric benchmarks where the two above-mentioned design parameters are distinguished in Sec.3.2 and 3.3: (i) the number of UCs and (ii) their scaling (or segmentation).

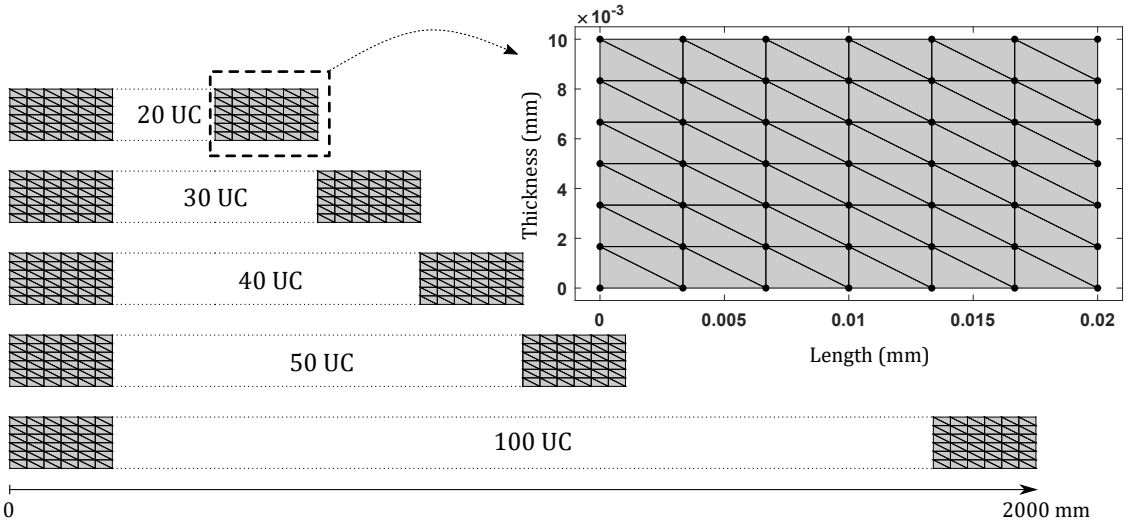

Figure 4: Description of the 5 FE models used for comparison between local and Floquet MOR techniques and detailed model of a single UC. The cell is made of aluminium, has a length d_x=20 mm, a thickness h=10 mm and is meshed using 49 nodes and 72 linear 2D triangular plane-strain elements with 2 translations per node, resulting in a total of 98 DOF.

3.2. Influence of the model's dimensions on the computational performances

To evaluate the effects of the number of UCs on the Local and Floquet MOR techniques, one can apply these methods to the five structures displayed in Fig.4. The structures are built by concatenating 20, 30, 40, 50 and 100 identical UCs, resulting in respectively: 400 mm, 600 mm, 800 mm, 1000 mm and 2000 mm-long structures. The constitutive UC is displayed in Fig.4. The size of each model is displayed in the 3^{rd} row of Tab.1. For each of these structures, five different strategies are used to conduct the same dynamic analysis: (a) the FEM with a full solver; (b) the FEM with an accelerated Sparse LU/Cholesky solver (SLU) (to exploit matrices' sparsity); the Local MOR using full (c) and SLU (d) solvers; and finally (e) the proposed Floquet MOR [1]. The dynamic analysis is a frequency response computation of the beam subjected to a left-side vertical force between 0 and 200 kHz. Identical reduction parameters are used for the local reduction, waves and component modes are kept up to $\omega_{\max} = 400$ kHz, the residues for the local UC and Floquet reductions are respectively set to $\varepsilon^{\mathrm{UC}} = 10^{-6}$ and $\epsilon^{\mathrm{Floq}} = 10^{-9}$.

[1] Although full solver is used as a benchmark, it is usually preferable to use SLU for FEM. However, this is not always true for Local MOR, which tends to produce full matrices.

Modelling/Solver		Number of UCs				
Method	Step duration (ms)	20	30	40	50	100
FEM	**Model size** (DOF)	**1694**	**2534**	**3374**	**4214**	**8414**
	Solving (full-ms/step)	197	562	1157	2295	15328
	Solving (SLU-ms/step)	7.92	12.2	16.7	21.1	46.4
Local MOR	**Model size** (DOF)	**494**	**734**	**974**	**1214**	**2414**
	ROM building (s)	0.61	1.50	3.16	6.2	43.15
	Solving (full-ms/step)	7.99	20.62	46.34	86.0	477.85
	Solving (SLU-ms/step)	1.25	2.80	3.60	4.70	11.19
Floquet MOR	**Model size** (DOF)	**92**	**134**	**179**	**220**	**353**
	ROM building (s)	2.05	2.20	2.60	2.70	4.24
	Solving (full-ms/step)	0.50	0.79	1.32	1.86	4.15

Table 1: Influence of the number of UCs (i.e. model size) on the performances of Local and Floquet MOR using full and reduced solvers. For each method, final number of DOF is indicated as well as the duration needed to reduce and solve the system. Note that the SLU-solver is not used for the Floquet MOR, since it produces full matrices. All computations are made on the same 2.90 GHz CPU limited to 16 Go RAM. The resolution time is averaged on 2000 frequency samples and expressed in sec./step.

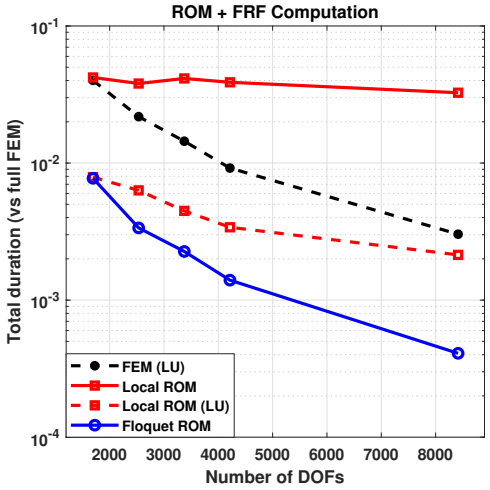

Figure 5: Reduction + 2000 FRF computations time vs. FEM full resolution. Number of DOF is proportionate to initial number of UCs.

Results are presented in Tab.1 and Fig.5. For a small number of UCs, Floquet and Local MOR are rather close in terms of solving performances, despite a significant difference in terms of model dimension. This is due to the high matrix sparsity of the Local MOR projection basis whereas the Floquet MOR produces full, yet 4-6 times smaller matrices. Still, as hypothesized in Sec.3.1, the gap between the two model-order reduction strategies increases with the number of UCs and DOF in the structure. When the number of UCs reaches 100, the Floquet MOR is more than 5 times faster than Local MOR. Oppositely, Local MOR loses its interest compared with FEM when using SLU solvers. This is due to the increasing time required to operate the projection matrices - which grow consistently with the number of UCs - due notably to the high number of state vectors required to reduce the UCs' interfaces.

To summarize, when the structure's size increases (i.e. the number of UCs, DOF, modes), the proposed Floquet MOR remains efficient without loss of benefits over FEM, while Local MOR becomes almost counter-productive as the length increases.

3.3. Influence of unit-cell's scaling on the computational performances

To evaluate the influence of the modelling scale on MOR efficiency, let us now consider the five models displayed in Fig.6. Given the waveguide's homogeneity one can define an arbitrary UC dimension to divide the 1000 mm-long aluminium structure into identical segments. It is therefore divided into 5, 20, 100, 250 and 500 UCs of respective

lengths 200 mm, 50 mm, 10 mm, 4 mm and 2 mm. Note that in all five cases the assembled FE model is strictly identical, namely a 34034 DOF model. The smallest constitutive UC is 1-element long (2 mm) and displayed in Fig.6. The dynamic analysis is conducted between 0 and 50 kHz with 1000 frequency samples and the load configuration, MOR residue parameters and CPU are the same as in Sec.3.2. Evanescent waves (filtered to $|\lambda| > 0.2$) are collected up to 100 kHz and component modes up to $\omega_{\max}$=150 kHz. Results are presented in Tab.2 and Fig.7.

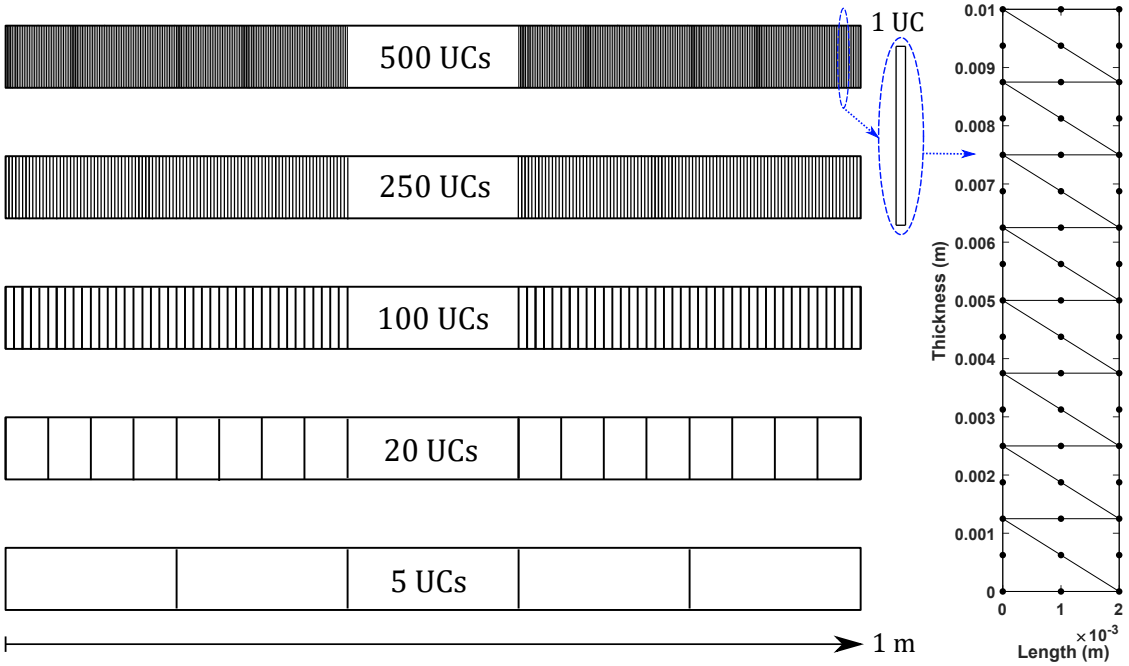

Figure 6: Description of a same structure modelled using 5 different segmentation. The cell has a length (1 element) d_x=2 mm, a thickness (8 elements) h=10 mm and is meshed using 51 nodes and 16 quadratic 2D triangular plane-strain (X,Y) elements, resulting in a total of 102 DOF. The number of section elements in the respective UCs (from top to bottom) is: 1, 2, 5, 25 and 100, respectively.

The overall duration (ROM building and resolution) of Local and Floquet MOR are displayed vs. FE modelling on the right-side curves axis of Fig.7. The two curves show that both methods are advantageous compared with FEM, although Floquet MOR clearly shows considerable reduction factor for any scaling value, while Local MOR looses efficiency above 250 segments: it grows from 3% to 25% of the total FEM time, meanwhile the cost of Floquet MOR decreases from 2% to 1%. These results are in accordance with the DOF reduction listed in Tab.2, which clearly show the stability of Floquet MOR against the increasing size of the model reduced through Local MOR. The bar diagram in Fig.7 indicates with a left-side axis the proportion of time dedicated to build the reduced model vs. the time required to compute the solution. It shows again that Floquet MOR is highly stable against the scaling choice and particularly that Floquet expansion and pole identification duration remain almost unchanged. The overwhelming effort is dedicated to build the reduced model, while the final model is extremely efficient for broadband/numerous resolutions. On the other hand, Local MOR shown balanced reduction vs. resolution efforts for 5 segments model,

while the resolution constitutes most of the computational effort for higher levels of the waveguide's segmentation.

Modelling/Solver		Number of divisions				
Method	Step	5	20	100	250	500
FEM	**Model size** (DOF)	**34034**				
	Solving-SLU (s)	460.9				
Local MOR	**Model size** (DOF)	**394**	**874**	**2423**	**6024**	**13026**
	UC reduction (s)	2.20	0.28	2.10	0.20	0.17
	Global projection	5.64	3.28	3.07	3.14	18.29
	Solving-SLU (s)	9.02	11.67	16.72	39.94	102.31
Floquet MOR	**Model size** (DOF)	**77**	**70**	**62**	**60**	**58**
	UC reduction (s)	1.85	0.29	1.93	0.20	0.18
	Poles identification (s)	5.28	4.55	2.77	3.21	2.98
	Floquet expansion (s)	1.56	1.26	1.16	1.24	1.42
	Projection (s)	0.31	0.28	0.25	0.25	0.24
	Solving (s)	0.40	0.35	0.26	0.25	0.26

Table 2: Detailed performances of each of the MOR algorithms and FEM simulation. The three methods (FEM with SLU resolution algorithm, Local MOR with SLU resolution algorithm, Floquet MOR) are implemented, resulting in the given model size (in DOF) while the ROM step duration is indicated for each method and UC scaling. Given the size of this model, only SLU-solvers could be used for FEM and local MOR comparisons, so as not to exceed computational and memory resources.

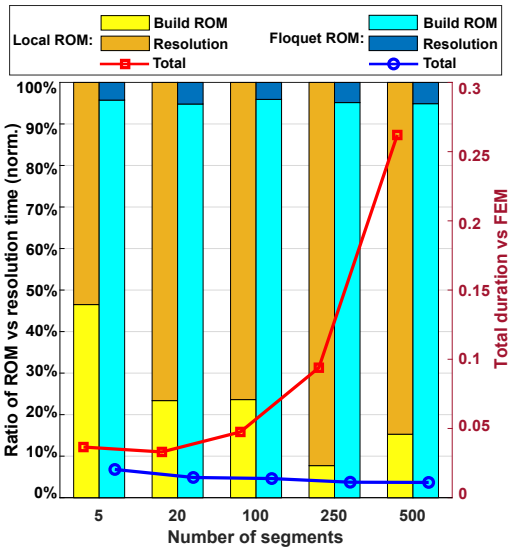

Figure 7: (a) Reduction + resolution time of local and Floquet MOR methods vs. FEM (right axis). (b) Bar diagram indicating the proportion of time dedicated to build reduced model vs. resolution (left axis).

To summarize, this parametric analysis shows that the Floquet MOR is always significantly faster than the alternatives for both reduction and resolution, reaching over 99% reduction compared with accelerated FEM (i.e. with SLU-solver). This conclusion stands, notwithstanding the segmentation of the structure. In fact, the Floquet MOR efficiency further increases with segmentation, in opposition to Local MOR which is more suited to lower levels of multiscality.

4. Application: transient response of a periodic structure

4.1. Description of the model

In this section the performances of both methods are studied for the computation of the transient dynamic response of a simple example of elastic metamaterial: the structure is a slender aluminium phononic-type waveguide with 30 elliptic inclusions producing both Bragg and locally-resonant bandgaps. A detailed description of the example's geometry, FE model and load configuration is provided in Fig.8.

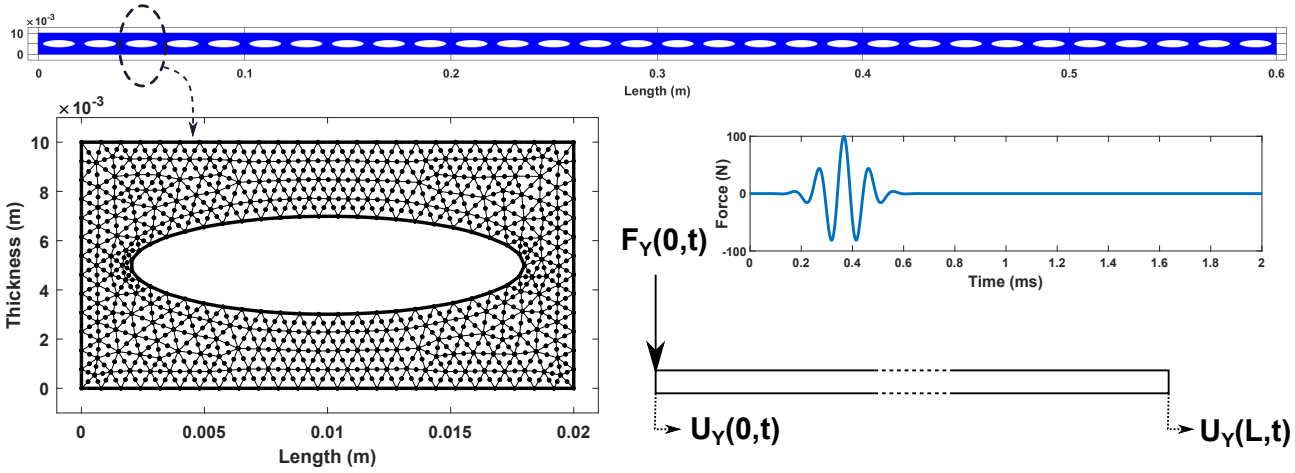

Figure 8: Application example of the 30-UC structure and detailed FE model of a single UC. The structure is made of aluminium (E=70 GPa, ν=0.33, ρ=2700 kg.m^{-3}), has a length d_x=20 mm, a thickness h=10 mm and is meshed using 1197 nodes and 537 quadratic 2D triangular plane-strain (X,Y) elements, resulting in 2394 DOF per UC. Each periodic cell has a centered 16 mm per 4 mm elliptic inclusion. The overall model is made of 30 UCs and 70254 DOF.

The structure is subjected to three different force impulses applied along the vertical direction on the left boundary while the right end is free. The input signal is a Gaussian pulse $F(t)$ of amplitude F_0, center frequency ω_0, cut-off frequency t_c at truncating amplitude -100dB defined by:

$$F(t) = F_0 \cos\left(\omega_0(t - t_c)\right) \exp\left(\frac{-(t - t_c)^2}{2\sigma^2}\right) \tag{26}$$

where $\sigma = \dfrac{1}{2\pi f_v}$ and f_v are respectively the Gaussian pulse's temporal and spectrum bandwidth variances. Displacements are then monitored at both ends over a duration of 2 ms.

4.2. Time integration and resolution

A direct time integration is used to solve the second order differential equation, based on Newmark method [25]. The numerical scheme used below is implicit and a constant acceleration scheme (i.e. unconditionally stable) is used by specifying $\alpha = \dfrac{1}{4}$ and $\delta = \dfrac{1}{2}$ in the integration constants defined as:

$$\begin{cases} a_0 = \dfrac{1}{\alpha\Delta^2}, \quad a_1 = \dfrac{\delta}{\alpha\Delta}, \quad a_2 = \dfrac{1}{\alpha\Delta}, \quad a_3 = \dfrac{1}{2\alpha} - 1 \\ a_4 = \dfrac{\delta}{\alpha} - 1, \quad a_5 = \Delta\left(\dfrac{\delta}{2\alpha} - 1\right), \quad a_6 = \Delta(1 - \delta), \quad a_7 = \Delta\delta \end{cases} \tag{27}$$

where Δ is the selected time step.

Defining K_{eff} the global effective stiffness matrix defined by: $K_{\text{eff}} = a_0\mathcal{M} + a_1\mathcal{C} + \mathcal{K}$ and denoting U_T, V_T, A_T the approximations of respective displacement state vectors' derivatives $\dfrac{\partial^2\mathcal{U}(t)}{\partial t^2}$, $\dfrac{\partial\mathcal{U}(t)}{\partial t}$ and $\mathcal{U}(t)$, the following iterative procedure can be used to solve the linear system subjected to the time-dependent load:

- The effective load vector is computed using:

$$R_{T+\Delta} = \mathcal{F}(T+\Delta) + \mathcal{M}\left[a_0 U_T + a_2 V_T + a_3 A_T\right] + C\left[a_1 U_T + a_4 V_T + a_5 A_T\right], \tag{28}$$

- The displacement state vector at time $T + \Delta$ is computed by:

$$U_{T+\Delta} = \hat{K}_{\text{eff}}^{-1} R_{T+\Delta}, \tag{29}$$

  where $\hat{K}_{\text{eff}}$ is a factorisation of K_{eff} into lower - upper triangular matrices.

- The velocities and accelerations are derived using:

$$\begin{cases} A_{T+\Delta} = a_0\left(U_{T+\Delta} - U_T\right) - a_2 V_T - a_3 A_T \\ V_{T+\Delta} = V_T + a_6 A_T + a_7 A_{T+\Delta}, \end{cases} \tag{30}$$

- The previous steps are resumed using the time step increment: $T = T + \Delta$

The time resolution is adapted to the different load cases described in the following, based on the highest frequency content of their normalized input spectrum above a 10^{-4} threshold.

4.3. Dynamic response, wave dispersion and spectra

First, wave dispersion characteristics are shown in Fig.9b. Four main propagating solutions are displayed, including the main (1) transverse vertical (i.e. flexural/A_0) wave. Although the vertical nature of the load is expected to generate mainly Wave 1, it is reminded that A_0 waves are not only transversely polarized in the considered bandwidth, hence the structure's response to a vertical load is multimodal. Wave 2 is the longitudinal/S_0 wave and creates a local resonance between 40 kHz and 50 kHz, while Waves 3 and 4 are two decaying waves coupled respectively with the longitudinal and flexural ones. Consider the three bandwidth P1, P2 and P3 shown in Fig. 9b. Wave 1 is propagating between 0 and 20 kHz (P1) then reaches the first Bragg region responsible for a stopband between 20 kHz and 42 kHz (P2). Above, a narrow pass-band (P3) is visible up to 53 kHz followed by a local resonance creating a second stopband up to 75 kHz. Three pulses are considered, respectively centered in P1 (1^{st} pass-band), P2 (stop-band) and P3 (2^{nd} pass-band) to test the reliability of the ROM inside the different pass- and stop-bands.

The Frequency Response Function (FRF) of the overall structure subjected to F_0 is shown in Fig.9a at two locations: co-localized (x=0) and at the end (x=L), along with the normalized spectra of the three pulses. The consequences of stop- and pass-bands are distinctly visible on the co-localized response (i.e. by the absence of resonant modes), and at the end point (i.e. by the amplitude drop).

To test the validity limit of the methods, a single ROM is built based on the criteria defined in Sec.2 with a single maximal frequency of 100 kHz. To account for the absence of poles in region P2, a regular frequency sampling was used to achieve the POD. The response of the structure to the three input signals defined by Pulses 1, 2 and

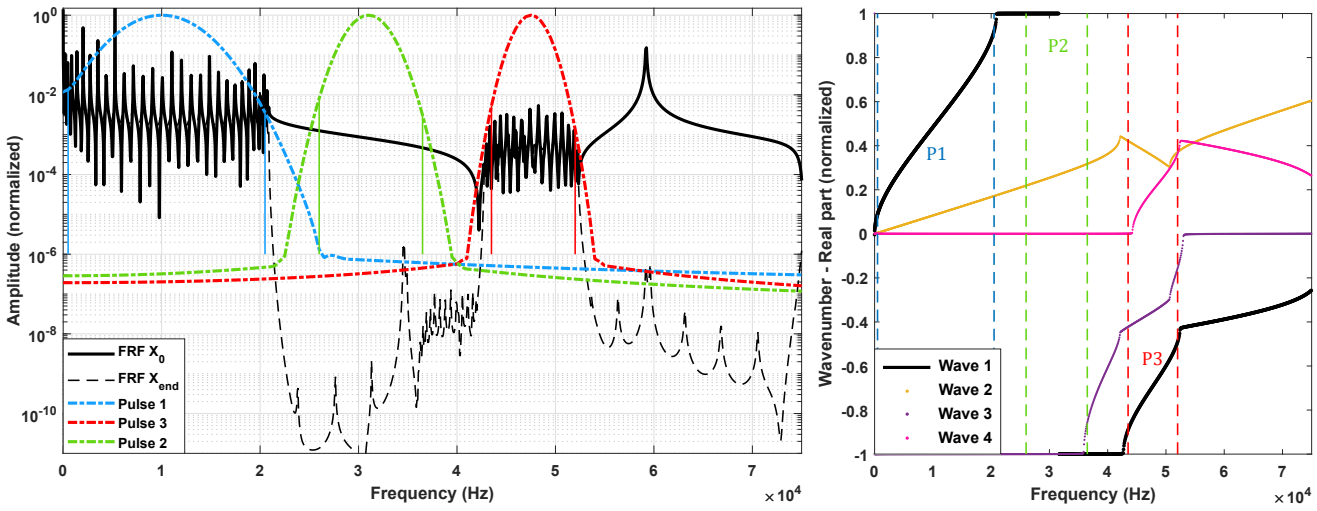

Figure 9: (a) Frequency response function at input force location (co-localized), and at the end of the structure (x=L). Frequency spectra of pulses 1, 2 and 3 are overlaid. (b) Wave dispersion characteristics (real wavenumber parts), showing 4 propagating waves in the considered bandwidth, and corresponding bandwidths of the three pulses in the various pass- and stop-bands. Wave 1 is mainly actuated, although all waves (including evanescent) are produced by load.

3 is computed using FEM and both MOR methods. A detailed description of each input signal's center frequency, fractional bandwidth ratio and time sampling is provided in the caption of Tab.3. Since the accuracy of the reduced model tends to decrease with frequency, it means that the model is expected to produce highly accurate results for both P1 and P2 and a slightly increased error for P3, whose spectrum extents closer to the upper validity limit of the ROM.

4.4. Results and accuracy

The computational efforts and DOF reduction produced by the two methods are detailed in Tab.3. The Floquet MOR produces a system of 160 DOF against the 70254 DOF of the initial FEM. Noteworthy, both reduction techniques are preferable to FEM in the three analyses, both in terms of computation time and model dimension. Interestingly, both Local and Floquet MOR take about the same time to create a reduced model. In fact, although the UC reduction is identical in both methods, the additional cost of Floquet MOR (i.e. for pole identification and Floquet expansion) is counterbalanced by its fast projection time on a much smaller basis. Overall, is it clear that the performances of Floquet MOR are far superior to FEM and to Local MOR. For the more expensive (i.e. Pulse 3) analysis, a resolution with Floquet MOR runs over 35× faster than Local MOR and 550× faster than FEM.

Accuracy is a crucial criterion to assess the performances of the reduced-order modelling techniques. Denoting $\mathcal{U}_{FEM}(t)$ and $\mathcal{U}_{ROM}(t)$ the global nodal displacement fields computed using FEM and Local or Floquet MOR respectively, the overall time-dependent reduction error is evaluated using the Modal Assurance Criterion residue defined by:

$$\varepsilon(t) = 1 - \frac{\mathcal{U}_{\mathrm{FEM}}(t) \cdot \mathcal{U}_{\mathrm{ROM}}(t)}{\|\mathcal{U}_{\mathrm{FEM}}(t)\| \, \|\mathcal{U}_{\mathrm{ROM}}(t)\|} \tag{31}$$

		Pulse 1	Pulse 2	Pulse 3	Model size
Method	Steps and duration	1201	3721	5701	(DOF)
FEM	Resolution (s)	**137.41**	**425.89**	**656.71**	70254
Local MOR	Building ROM (s)	17.25			2064
	Resolution (s)	**9.05**	**27.35**	**42.31**	
Floquet MOR	Building ROM (s)	16.96			160
	Resolution (s)	**0.42**	**1.02**	**1.15**	

Table 3: Computational effort of the different modelling techniques. For Local and Floquet reduction, the time dedicated to build the ROM is distinguished from the resolution time. Pulse P1 has a center-frequency $\omega_0^{(1)}$=10 kHz and a fractional bandwidth ratio of 20%, in order to have a spectrum covering the most part of the first pass-band. Pulse P2 is centered on $\omega_0^{(2)}$=31 kHz with a bandwidth ratio of 5% to be fully contained in the stop-band. Pulse P3 is centered on $\omega_0^{(3)}$=47.5 kHz with a 2.5% bandwidth ratio, corresponding to the 2^{nd} pass-band. In each case, the input amplitude is F_0=100 N and the simulation duration is 2 ms. The time resolution is set to guarantee a sampling frequency of 3× the center frequency of the signal, i.e. 30 kHz for P1 ($\Delta^{(1)}$=1.67μs), 93 kHz for P2 ($\Delta^{(2)}$=0.54μs) and 142.5 kHz for P3 ($\Delta^{(3)}$=0.35μs).

where $\cdot$ is the scalar product and $\|\,\|$ the L^2-norm. The errors produced by both methods on P1, P2 and P3 analyses are displayed in Fig.10. In the P3 input case, an additional analysis was conducted, extending the duration up to 2 $t_{\max}$ in order to observe the time convergence of the error.

Firstly, one can note the outstanding accuracy of Floquet MOR for P1 and P2 analyses. The error on P3 is slightly higher over time as expected, although it remains accurate for the first 1 ms and still converges around 3% at 4 ms. Second, one clearly identifies regular peaks on all MAC plots. These times are corresponding to the reflection of the pulses on the edges of the structure. A possible explanation for this phenomenon is that each reflection on a boundary generates a variety of evanescent or highly decaying waves which the ROM fails to describe accurately. The absence of such error peaks for P2 (i.e. inside the bandgap) tends to support this interpretation. These discrepancies however vanish with the far field, probably due to the attenuation. One can thirdly observe that both Floquet MOR and Local MOR produce very similar errors. Interestingly, this can be interpreted as the consequence of their shared wave-mode decomposition prerequisite, inherent to these method (i.e. based on a frequency truncation) and possibly responsible for a poor projection of the waveguide's interfaces. The proposed Floquet MOR thus does not produce any additional error.

The time-dependent upper surface nodal displacements on the two locations (defined in Fig.8) $\mathbf{U}_Y(0,t)$ and $\mathbf{U}_Y(L,t)$ are displayed for each input signal in Fig.11. The reduced model produces a highly accurate response without any observable discrepancy over FEM, either on the source point and 30 UC further, at the end of the structure. The low frequency components, which are sometimes inadequately described by a reduced wave decomposition and here appear a translation motion (e.g. top-right in Fig.11), are also perfectly approximated by the Floquet MOR method. Noteworthy, the response to signal P2 (i.e. inside the stop-band) at $x = L$ (middle-right in Fig.11) is also accurately

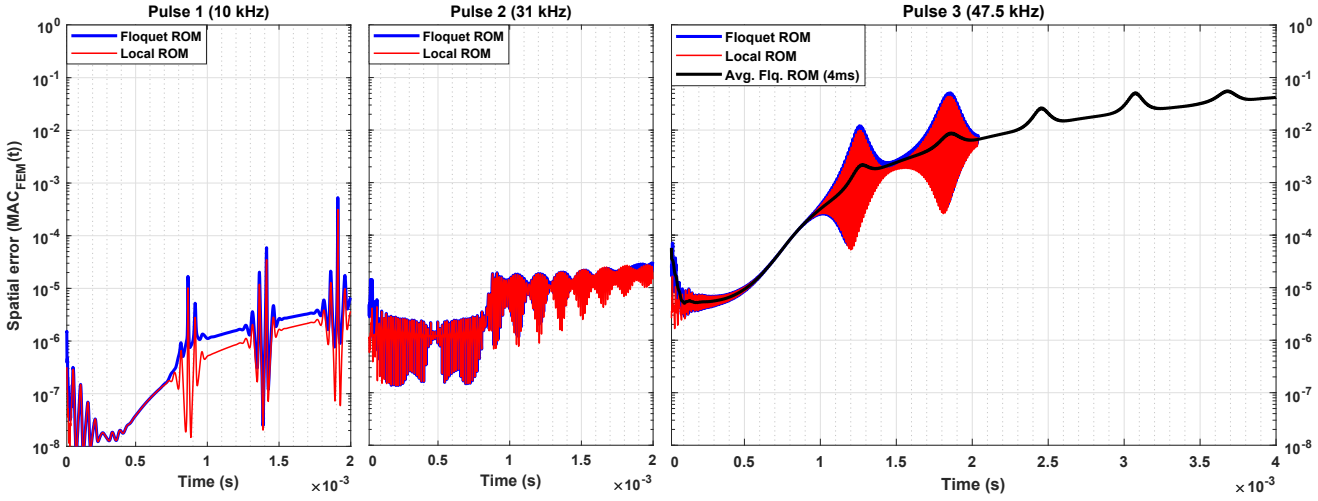

Figure 10: Time dependence estimation of the global error produced by Floquet and Local MOR methods using full field MAC over FEM results. Convergence is shown to be attained with higher simulation duration for Pulse 3, and is established around -3%.

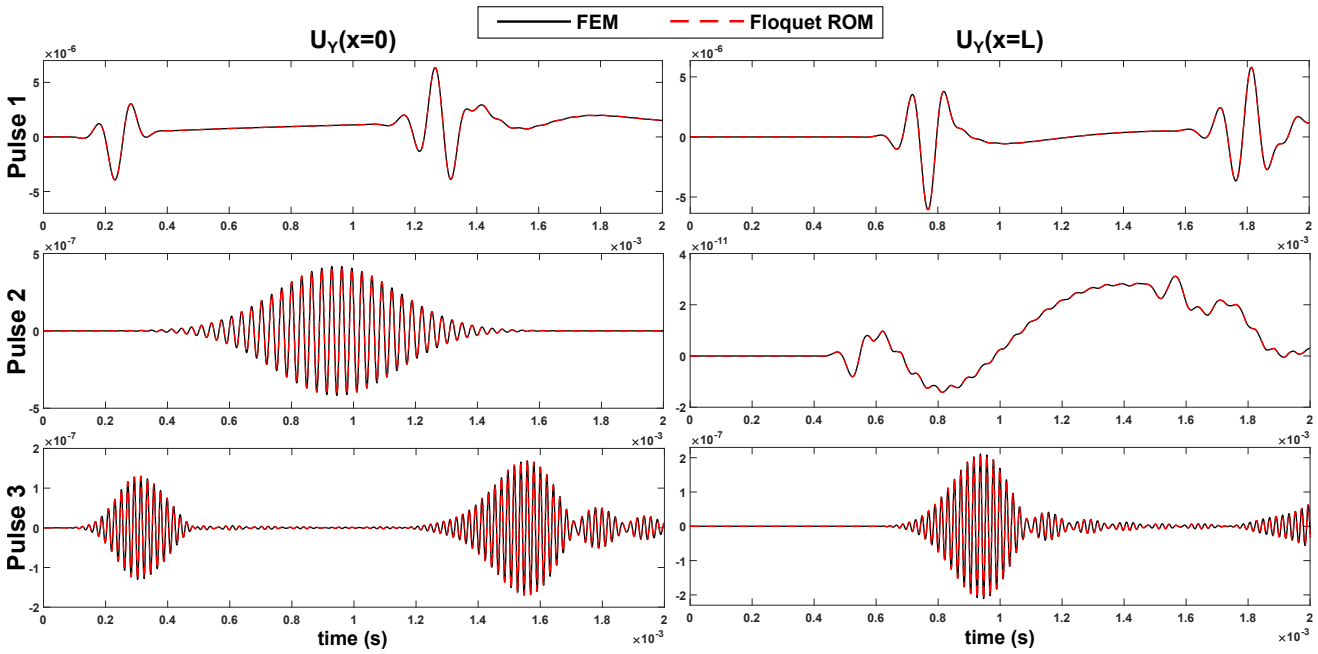

Figure 11: Time signals comparison at two different locations for the three pulse's inputs.

described with the reduced model, although this is a residual displacement resulting from second-order and converted waves propagating through the 30 UCs. The fact that the Floquet MOR maintains high accuracy above the first Brillouin zone, both inside and outside bandgaps is remarkable and should be emphasized. Moreover, for the smallest signal's wavelength (P3, bottom in Fig.11) which is the upper limit of the Floquet MOR validity bandwidth, the

discrepancy with FEM remains invisible, despite the increased MAC error mentioned earlier. One can reasonably deduce that the method is still efficient and remains highly accurate up to the upper bandwidth used to generate the reduced model.

5. Conclusions

A Floquet MOR method was investigated in this paper, with the objective to create small and accurate ROM of periodic structures which can be used for time domain applications. A global frequency-independent projection matrix was built from a POD-like basis construction strategy and a Floquet expansion of local state-vectors. By leveraging the outstanding performances of the forced WFEM framework, the proposed Floquet MOR quickly generates an accurate ROM. Comparing an extension of a local reduction strategy (i.e. local MOR) to the Floquet MOR, the authors demonstrated a clear added value of the latter, which can be summarized as follows:

- Floquet MOR is considerably faster than local MOR, notwithstanding sparsity of the system or the solver used.
- The resulting reduced model is extremely small and nearly minimal given the number of modes in the bandwidth.
- Floquet MOR is less sensitive, if at all, to a change of the modeling scale or the number of unit-cells in the structure.

Still, some aspects of the method could be further investigated, as it was observed for example that the Floquet MOR is not strictly insensitive to the scaling. This means that a better trade-off could be sought between the snapshots sampling procedure and the SVD residue threshold. In time-domain applications, small spikes of the MAC error were also identified during interface reflections. Excluding the boundary cells from the reduction could therefore contribute to reduce near-field ROM discrepancies.

It is expected that Floquet MOR will be highly valuable in fields such as virtual sensing, real-time SHM and digital twins, by providing a unit-cell-based MOR technique, exploitable for the time-domain analysis of large-scaled finite periodic structures and metamaterials.

CRediT author statement

Christophe Droz: Original concept, Method, Software, Investigation, Writing- Original draft, Funding acquisition. **Regis Boukadia**: Method, Investigation, Writing- review & editing. **Wim Desmet**: Critical review, Project supervision

Acknowledgements

This work was funded by the European Union's Horizon 2020 research and innovation programme, through the individual Marie Skłodowska-Curie fellowship of Christophe Droz (WIDEA) [grant number 797034]. The research of R. F. Boukadia is funded by an Early Stage Researcher grant within the European Project VIPER Marie Curie Initial Training Network [grant number 675441] and the KU Leuven Industrial Research Fund (IOF).

References

[1] W. C. Hurty, Dynamic analysis of structural systems using component modes, AIAA journal 3 (4) (1965) 678–685.

[2] B. Besselink, U. Tabak, A. Lutowska, N. van de Wouw, H. Nijmeijer, D. J. Rixen, M. Hochstenbach, W. Schilders, A comparison of model reduction techniques from structural dynamics, numerical mathematics and systems and control, Journal of Sound and Vibration 332 (19) (2013) 4403–4422.

[3] D. de Klerk, D. J. Rixen, S. Voormeeren, General framework for dynamic substructuring: history, review and classification of techniques, AIAA journal 46 (5) (2008) 1169–1181.

[4] F. A. Lülf, D.-M. Tran, R. Ohayon, Reduced bases for nonlinear structural dynamic systems: A comparative study, Journal of Sound and Vibration 332 (15) (2013) 3897–3921.

[5] M. Kapteyn, D. Knezevic, D. Huynh, M. Tran, K. Willcox, Data-driven physics-based digital twins via a library of component-based reduced-order models, International Journal for Numerical Methods in Engineering (2020).

[6] S. van Ophem, E. Deckers, W. Desmet, Model based virtual intensity measurements for exterior vibro-acoustic radiation, Mechanical Systems and Signal Processing 134 (2019) 106315.

[7] A. van de Walle, F. Naets, W. Desmet, Virtual microphone sensing through vibro-acoustic modelling and kalman filtering, Mechanical Systems and Signal Processing 104 (2018) 120–133.

[8] J.-Z. Huang, D.-S. Li, C. Zhang, H.-N. Li, Improved kalman filter damage detection approach based on lp regularization, Structural Control and Health Monitoring 26 (10) (2019) e2424.

[9] D. Mead, A general theory of harmonic wave propagation in linear periodic systems with multiple coupling, Journal of Sound and Vibration 27 (2) (1973) 235–260.

[10] R. F. Boukadia, C. Droz, M. N. Ichchou, W. Desmet, A bloch wave reduction scheme for ultrafast band diagram and dynamic response computation in periodic structures, Finite Elements in Analysis and Design 148 (2018) 1–12.

[11] M. Mallouli, M. B. Souf, O. Bareille, M. Ichchou, T. Fakhfakh, M. Haddar, Damage detection on composite beam under transverse impact using the wave finite element method, Applied Acoustics 147 (2019) 23–31.

[12] M. K. Malik, D. Chronopoulos, G. Tanner, Transient ultrasonic guided wave simulation in layered composite structures using a hybrid wave and finite element scheme, Composite Structures (2020) 112376.

[13] C. Droz, J.-P. Lainé, M. Ichchou, G. Inquiété, A reduced formulation for the free-wave propagation analysis in composite structures, Composite Structures 113 (2014) 134–144.

[14] C. Droz, C. Zhou, M. Ichchou, J.-P. Lainé, A hybrid wave-mode formulation for the vibro-acoustic analysis of 2d periodic structures, Journal of Sound and Vibration 363 (2016) 285–302.

[15] D. Krattiger, M. I. Hussein, Generalized bloch mode synthesis for accelerated calculation of elastic band structures, Journal of Computational Physics 357 (2018) 183–205.

[16] A. Palermo, A. Marzani, A reduced bloch operator finite element method for fast calculation of elastic complex band structures, International Journal of Solids and Structures 191 (2020) 601–613.

[17] D. Beli, J.-M. Mencik, P. Silva, J. Arruda, A projection-based model reduction strategy for the wave and vibration analysis of rotating periodic structures, Computational Mechanics 62 (6) (2018) 1511–1528.

[18] Y. Fan, C. Zhou, J. Laine, M. Ichchou, L. Li, Model reduction schemes for the wave and finite element method using the free modes of a unit cell, Computers & Structures 197 (2018) 42–57.

[19] D. Krattiger, L. Wu, M. Zacharczuk, M. Buck, R. J. Kuether, M. S. Allen, P. Tiso, M. R. Brake, Interface reduction for hurty/craig-bampton substructured models: Review and improvements, Mechanical Systems and Signal Processing 114 (2019) 579–603.

[20] H. Pinault, E. Arlaud, E. Balmes, A general superelement generation strategy for piecewise periodic media, Journal of Sound and Vibration 469 (2020) 115133.

[21] R. Hu, C. Oskay, Spectral variational multiscale model for transient dynamics of phononic crystals and acoustic metamaterials, Computer Methods in Applied Mechanics and Engineering 359 (2020) 112761.

[22] R. V. Patel, On computing the eigenvalues of a symplectic pencil, Linear algebra and its applications 188 (1993) 591–611.

[23] G. W. Stewart, A krylov–schur algorithm for large eigenproblems, SIAM Journal on Matrix Analysis and Applications 23 (3) (2002) 601–614.

[24] R. M. Larsen, Lanczos bidiagonalization with partial reorthogonalization, DAIMI Report Series (537) (1998).

[25] N. M. Newmark, A method of computation for structural dynamics, Journal of the engineering mechanics division 85 (3) (1959) 67–94.